Available online at www.sciencedirect.com

ScienceDirect

Advances in Space Research 77 (2026) 9382–9400

ADVANCES IN SPACE RESEARCH (a COSPAR publication)

www.elsevier.com/locate/asr

Nanosatellite attitude estimation, in-orbit sensor calibration and fault detection using kinematic relations only

Chingiz Hajiyev [a,*], Demet Cilden-Guler [b]

[a] Department of Aeronautical Engineering, Istanbul Gelisim University, Turkiye
[b] Department of Mechanical and Manufacturing Engineering, University of Calgary, Canada

Received 31 October 2025; received in revised form 3 February 2026; accepted 11 March 2026
Available online 16 March 2026

Abstract

This study focuses on estimating the attitude angles of a nanosatellite using vector measurements from onboard magnetometers and sun sensors. The estimation scheme employs a nontraditional filtering approach that relies solely on a kinematic model propagated with gyroscope and magnetometer data. The overall process consists of two main stages. In the first stage, attitude measurements are obtained using a single frame method based on singular value decomposition (SVD). In the second stage, these measurements are fused within an Extended Kalman Filter (EKF) that incorporates a linearized attitude model together with nonlinear magnetometer observations. Integrating these two stages yields a unified estimation scheme, referred to as the SVD Aided EKF, which enables accurate, simultaneous estimation of attitude angles as well as gyroscope and magnetometer biases. To detect attitude sensor faults, this study proposes fault detection statistics based on the central Wishart matrix whose diagonal elements are obtained from the components of the innovation vector. The proposed innovation-based fault detection algorithm was applied to the SVD-Aided EKF attitude estimation system to detect nanosatellite attitude sensor faults.

Keywords: Nanosatellite; Attitude estimation; Kinematics; Extended Kalman filter; Singular value decomposition; Fault detection

1. Introduction

The orientation of a satellite can be estimated using Kalman filtering techniques by combining body-frame measurements with known reference vectors. Conventional approaches for estimating a satellite's attitude angles and angular rates within an Extended Kalman Filter (EKF) or an Unscented Kalman Filter (UKF) framework typically rely on nonlinear vector observations, as the measurement models are inherently nonlinear (Lefferts et al., 1982, Markley et al., 2005; Crassidis et al., 2007; Hajiyev and Soken, 2014; Kramlikh et al., 2023). Alternatively, linear measurement-based methods use attitude estimates obtained through single-frame attitude determination techniques (Cilden-Guler et al., 2017). These techniques calculate the attitude independently at each time step using vector observations and are then incorporated into the Kalman filter as direct measurement inputs (Hajiyev and Bahar, 2003; Hajiyev and Cilden, 2016; Hajiyev et al., 2016; Soken and Sakai, 2019; Hajiyev and Cilden-Guler, 2021; Boussadia et al., 2022; Mmopelwaet al., 2023). Having state measurements directly from the single-frame method makes the measurement model linear. Filters employing this method are often referred to as single-frame method-aided filters.

* Corresponding author.
E-mail addresses: chacizade@gelisim.edu.tr (C. Hajiyev), demet.cildenguler@ucalgary.ca (D. Cilden-Guler).

https://doi.org/10.1016/j.asr.2026.03.046

To propagate the satellite's orientation within the filter, either a kinematic model alone or a combination of kinematic and dynamic models can be employed. However, dynamics-based models often introduce modeling errors, particularly due to uncertainties in parameters such as the satellite's inertia matrix (Crassidis et al., 2007). This limitation has led to the development of algorithms that rely solely on kinematics, thereby avoiding errors linked to uncertain dynamics.

There are two principal strategies for satellite attitude and angular rate estimation: *(i)* approaches based solely on kinematic equations, and *(ii)* approaches that incorporate both kinematic and dynamic equations. Replacing a gyro-driven propagation model with one based on rotational dynamics enables the removal of onboard gyroscopes, but this substitution requires an accurate and reliable dynamics model. The study in (Cilden-Guler and Hajiyev, 2023) explores this trade-off by analyzing the threshold of uncertainty in the satellite's mass moment of inertia beyond which the benefits of using a dynamics-based model diminish.

In this context, we present a single-frame method-aided filtering approach that operates with both kinematic-only and combined kinematic-dynamic models. The method is particularly suitable for small satellites, where the accuracy of the inertia matrix may degrade over time. Simulation results demonstrate that when there is no uncertainty in the inertia matrix, the combined model offers superior estimation of gyro biases. However, as uncertainties increase—particularly beyond a 3% deviation in the principal moments of inertia—the purely kinematics-based filter achieves better performance. Therefore, for small satellite missions where inertia uncertainties are expected to evolve over time, kinematics-only attitude estimation provides a more robust and reliable solution by mitigating the impact of uncertain dynamic parameters.

Satellite attitude estimation based solely on kinematics using angular rate gyroscopes and vector measurements is presented in (Cilden-Guler and Hajiyev, 2023; Zhang et al., 2020; Liu et al., 2022). In these studies, satellite attitude angles or quaternions, as well as rate gyro biases, are estimated based on the EKF or multiplicative extended Kalman filter (MEKF). Orbital calibration of attitude sensors and fault detection/isolation issues were not addressed in these publications. To successfully complete a space mission, it is important to quickly detect the attitude sensor faults in real time. With the aid of Kalman filter innovations, flaws in dynamical systems can be identified and detected. The pioneering research in this field can be traced to the methodology proposed in (Mehra and Peschon, 1971).

When the system is functioning normally, the normalized innovation sequence of the Kalman filter has the characteristic of being Gaussian white noise with a unit covariance matrix and zero mean. The faults in the system alter the characteristics of the normalized innovation sequence. Methods for testing the conformity of an innovation sequence to white noise and for identifying changes in its expectation are based on traditional statistical methods (Mehra and Peschon, 1971). Testing the innovation covariance matrix of a Kalman filter in real time has proven to be a challenging and underdeveloped problem because determining the confidence region for a random matrix is difficult. In practice, one uses a scalar measure of this matrix, such as the trace (Mehra and Peschon, 1971), sum of the matrix elements (Hajiyev, 2010, 2014), determinant (Gordon, 1989; Gadzhiyev, 1994), matrix eigenvalues (Gadzhiyev, 1996; Hajiyev, 2010), etc.

In this study, attitude estimation, in-orbit calibration of attitude sensors and fault detection issues are addressed together using only kinematic relations. We propose a single-frame method-aided filter that relies fully on the kinematic model, omitting the use of satellite dynamics, making it well-suited for nanosatellite applications. The singular value decomposition (SVD) method was used as a single frame method to determine the satellite attitude using magnetometer and sun sensor measurements. In the filter called SVD-Aided EKF, the SVD-derived attitude angles are taken as input measurements in the EKF. The SVD-Aided EKF concurrently estimates the attitude angles, as well as the biases of the gyroscope and magnetometer. To detect sensor faults, this study proposes fault detection statistics based on the central Wishart matrix derived from the innovations of the SVD-Aided EKF. The proposed innovation-based sensor fault detection algorithm was applied to the attitude estimation system to detect the faults of attitude sensors.

2. Mathematical models

2.1. Attitude kinematics

The kinematic equations can be written using Euler angles as follows (Wertz, 2002):

$$\begin{bmatrix} \dot{\phi} \\ \dot{\theta} \\ \dot{\psi} \end{bmatrix} = \begin{bmatrix} 1 & s(\phi)t(\theta) & c(\phi)t(\theta) \\ 0 & c(\phi) & -s(\phi) \\ 0 & s(\phi)/c(\theta) & c(\phi)/c(\theta) \end{bmatrix} \begin{bmatrix} p \\ q \\ r \end{bmatrix}, \tag{1}$$

where $c(\cdot)$, $s(\cdot)$ and $t(\cdot)$ are the cosine, sine and tangent functions, ϕ, θ, ψ are the yaw, pitch, and roll angles respectively, and p, q, r are the components of the $\bar{\omega}_{BR}$ vector of the body frame with respect to the reference frame.

2.2. Gyro measurement model

The rate gyro measurements can be modelled as,

$$\omega_{BI_m}(j) = \omega_{BI}(j) + \eta_g(j) + b_g(j) \tag{2}$$

where $\omega_{BI}(j) = [\,\omega_x(j) \quad \omega_y(j) \quad \omega_z(j)\,]^T$ is the angular velocity vector of the body frame with respect to the inertial frame, $b_g(j)$ is the gyro bias vector and $\eta_g(j)$ is the normally distributed white noise with zero mean and variance,

$$E\left[\eta_g(j)\eta_g^T(k)\right] = I_{3x3}\sigma_g^2\delta(jk), \tag{3}$$

where I_{3x3} is the identity matrix with the dimension of 3×3,$\delta(jk)$ is the Kronecker delta function, σ_g is the standard deviation of the rate gyro error. The gyro bias $b_g(j) = \begin{bmatrix} b_{g_x}(j) & b_{g_y}(j) & b_{g_z}(j) \end{bmatrix}^T$ characteristic is:

$$b_g(j+1) = b_g(j) + \eta_1(j) \times \Delta t \tag{4}$$

where $\eta_1(j)$ is the normally distributed white noise with zero mean and variance,

$$E\left[\eta_1(j)\eta_1^T(k)\right] = I_{3x3}\sigma_{gb}^2\delta(jk), \tag{5}$$

where σ_{gb} is the standard deviation of the gyro biases.

2.3. Magnetometer measurement model

The satellite's three onboard magnetometers measure the components of the Earth's magnetic field vector in the body frame. The general measurement model can be defined as;

$$\begin{bmatrix} B_{mx}(j) \\ B_{my}(j) \\ B_{mz}(j) \end{bmatrix} = \left(A \begin{bmatrix} B_{ox}(j) \\ B_{oy}(j) \\ B_{oz}(j) \end{bmatrix} + b_m(j) + \eta_m(j) \right) \tag{6}$$

where, $B_{ox}(j)$,$B_{oy}(j)$ and $B_{oz}(j)$ are the Earth geomagnetic field direction cosines in the orbit frame, $B_{mx}(j)$,$B_{my}(j)$ and $B_{mz}(j)$ are the measured Earth geomagnetic field direction cosines in the body frame, $b_m(j)$ is the magnetometer bias vector as $b_m(j) = \begin{bmatrix} b_{m_x}(j) & b_{m_y}(j) & b_{m_z}(j) \end{bmatrix}^T$ and $\eta_m(j)$ is the zero mean Gaussian white noise with the covariance matrix of

$$E\left[\eta_m(j)\eta_m^T(k)\right] = I_{3x3}\sigma_m^2\delta(jk) = R_m(j) \tag{7}$$

where σ_m is the standard deviation of the magnetometer error. The characteristic of magnetometer biases $b_m(j) = \begin{bmatrix} b_{m_x}(j) & b_{m_y}(j) & b_{m_z}(j) \end{bmatrix}^T$ is given as,

$$b_m(j+1) = b_m(j) + \eta_2(j) \times \Delta t \tag{8}$$

where $\eta_2(j)$ is the normally distributed white noise with zero mean and variance,

$$E\left[\eta_2(j)\eta_2^T(k)\right] = I_{3x3}\sigma_{mb}^2\delta(jk), \tag{9}$$

where σ_{mb} is the standard deviation of the magnetometer biases.

2.4. Sun sensor measurement model

The unit sun direction vector in the Earth-Centered Inertial (ECI) frame can be computed using a linear model based on the sun's ecliptic longitude (Crassidis et al., 2007). After completing the transformation of the sun's unit direction vector from the ECI frame to the orbital frame, the model for the sun sensor measurements can be expressed as follows:

$$S_{mes}(j) = S_b = AS_o(j) + \eta_s(j), \tag{10}$$

where, $S_o(j)$ is the sun direction vector in the orbit frame and $S_b(j)$ are the sensor observations in the body frame that are distorted by $\eta_s(j)$, zero mean Gaussian white noise, which has the property of

$$E\left[\eta_s(j)\eta_s^T(k)\right] = I_{3x3}\sigma_s^2\delta(jk). \tag{11}$$

where σ_s is the standard deviation of the sun sensor measurement noise.

3. Single-frame attitude determination method

For the single-frame attitude determination method, the Singular Value Decomposition (SVD) approach was employed (Markley and Mortari, 2000). Since the SVD method is faster than the q-method and more robust than other faster methods such as FOAM (Fast Optimal Attitude Matrix) and ESOQ (EStimator of the Optimal Quaternion), it is considered an efficient single-frame method in the literature (Markley and Mortari, 2000; Cilden-Guler et al., 2017).

The loss is caused by the divergence of the measurements from the corresponding reference models

$$L(A) = \frac{1}{2}\sum_i a_i|b_i - Ar_i|^2 \tag{12}$$

$$B = \sum a_i b_i r_i^T \tag{13}$$

$$L(A) = \sum a_i - tr\left(AB^T\right) \tag{14}$$

where b_i is the measurement vector, r_i is the reference vector, a_i is the non-negative weight.

$$B = USV^T = U\mathrm{diag}([S_{11}S_{22}S_{33}])V^T \tag{15}$$

$$A_{opt} = Udiag[\,1 \quad 1 \quad \det(U)\det(V)\,]V^T \tag{16}$$

According to SVD, the U and V matrices are left and right orthogonal matrices. They use the principal singular values $(S_{11},\ S_{22},\ S_{33})$ to express the matrix B. The attitude matrix A_{opt} can be used to determine the Euler angle values. The attitude angle estimation errors' covariance matrix is

$$P_{SVD} = Udiag\left[\,(s_2+s_3)^{-1} \quad (s_3+s_1)^{-1} \quad (s_1+s_2)^{-1}\,\right]U^T \tag{17}$$

where $s_1 = S_{11}$ $s_2 = S_{22}$ $s_3 = \det(U)\det(V)S_{33}$.

4. SVD-aided EKF for attitude estimation

Gyroscopes, magnetometers and sun sensors are used as the attitude and rate sensors in this study. By using Earth's magnetic field and sun direction vectors in the SVD sub step, attitude angle measurements $Z_\phi(j)$, $Z_\theta(j)$, $Z_\psi(j)$ and the covariance matrix of measurement noise P_{SVD} are obtained. The Euler angle measurements can be written as [6],

$$\begin{aligned} Z_\phi(j) &= \phi(j) + v_\phi(j) \\ Z_\theta(j) &= \theta(j) + v_\theta(j) \\ Z_\psi(j) &= \psi(j) + v_\psi(j) \end{aligned} \tag{18}$$

where $v_{(.)}(k)$ is the measurement noise of the attitude angles. We can call the SVD measurements as $Z_1(j) = [\,Z_\phi(j) \quad Z_\theta(j) \quad Z_\psi(j)\,]^T$. The gyro measurements described in (2) can be expressed as $Z_2(j) = \omega_{BI_m}(j)$. The magnetometer measurements described in (6) can be written as $Z_3(j) = [\,B_{mx}(j) \quad B_{my}(j) \quad B_{mz}(j)\,]^T$. $Z_1(j)$ represents the measurements from SVD using the magnetometer and sun sensor measurements.

The augmented state vector in this case is

$$x(j) = [\,\phi(j) \quad \theta(j) \quad \psi(j) \quad b_{g_x}(j) \quad b_{g_y}(j) \quad b_{g_z}(j) \quad b_{m_x}(j) \quad b_{m_y}(j) \quad b_{m_z}(j)\,]^T \tag{19}$$

The Kalman filter uses only kinematics and measurements $Z(j) = [\,Z_1(j) \quad Z_3(j)\,]^T$ for attitude estimation and calibration of attitude sensors. This indicates that the attitude measurements from SVD $Z_1(j)$ and magnetometer measurements $Z_3(j)$ make up the measurement input vector. Consequently, the measurement vector $Z(j)$ consists of the output signals of the SVD and the nonlinear measurements of the magnetometers and can be written as follows:

$$Z(j) = [\,Z_\phi(j) \quad Z_\theta(j) \quad Z_\psi(j) \quad B_{mx}(j) \quad B_{my}(j) \quad B_{mz}(j)\,]^T \tag{20}$$

The corrected (bias eliminated) rate gyro measurements can be determined from the rate gyroscope measurements as $Z_2^{cor}(j) = Z_2(j) - \hat{b}_g(j-1)$ where $\hat{b}_g(j-1)$ is the estimated gyro bias vector by the filter. In this case, the covariance matrix of the corrected gyroscope measurement noise will be determined as follows:

$$E\left[\eta_g(j)\eta_g^T(k)\right] = \begin{bmatrix} \sigma_g^2 + Var\left(\hat{b}_{g_x}\right) & 0 & 0 \\ 0 & \sigma_g^2 + Var\left(\hat{b}_{g_y}\right) & 0 \\ 0 & 0 & \sigma_g^2 + Var\left(\hat{b}_{g_z}\right) \end{bmatrix} \tag{21}$$

Here $Var\left(\hat{b}_{g_x}\right)$, $Var\left(\hat{b}_{g_y}\right)$ and $Var\left(\hat{b}_{g_z}\right)$ are the variances of gyroscope bias estimation errors. After this procedure, the bias-free rate gyro measurements are fed back into the kinematics model which is also used in the SVD-Aided EKF.

Below, an SVD-Aided EKF algorithm is presented to estimate rotational motion parameters and attitude sensor biases, based on the defined system (1) and measurement vector (20).

The corrected (bias eliminated) magnetometer measurements can be represented from the magnetometer measurements as $Z_3^{cor}(j) = Z_3(j) - \hat{b}_m(j-1)$ where $\hat{b}_m(j-1)$ is the estimated magnetometer bias vector by the filter. In this case, the corrected covariance matrix of the magnetometer measurement noise is written in the following form:

$$E\left[\eta_m(j)\eta_m^T(k)\right] = R_m^{cor} = \begin{bmatrix} \sigma_m^2 + Var\left(\hat{b}_{m_x}\right) & 0 & 0 \\ 0 & \sigma_m^2 + Var\left(\hat{b}_{m_y}\right) & 0 \\ 0 & 0 & \sigma_m^2 + Var\left(\hat{b}_{m_z}\right) \end{bmatrix} \tag{22}$$

Here $Var\left(\hat{b}_{m_x}\right)$, $Var\left(\hat{b}_{m_y}\right)$,$Var\left(\hat{b}_{m_z}\right)$ are the variances of magnetometer bias estimation errors. The bias-free magnetometer measurements and the covariance matrix of the magnetometer measurement noise are then fed back into the SVD algorithm and measurement update part of EKF.

The discrete-time nonlinear state space model is used to formulate the satellite's rotational motion about its mass center

$$x(j+1) = f[x(j)] + w(j) \tag{23}$$

$$Z(j) = \begin{bmatrix} Z_1(j) \\ Z_3(j) \end{bmatrix} = \begin{bmatrix} H_1 x(j) + v_1 \\ h[x(j)] + b_m(j) + \eta_m(j) \end{bmatrix} \tag{24}$$

where $f[\cdot]$ and $h[\cdot]$ are the nonlinear kinematic and magnetometer measurement functions respectively, $w(j)$ is zero mean Gaussian noise with covariance $Q(j)$, $Z(j)$ is the 6-dimensional measurement vector, $v_1(j)$ is zero mean Gaussian noise with covariance $P_{SVD}(j)$, $\eta_m(j)$ is the zero-mean Gaussian noise with covariance (22), H_1 is the measurement matrix corresponding to the linear measurements (18) and can be expressed as,

$$H_1 = \begin{bmatrix} 1 & 0 & 0 & 0 & 0 & 0 & 0 & 0 & 0 \\ 0 & 1 & 0 & 0 & 0 & 0 & 0 & 0 & 0 \\ 0 & 0 & 1 & 0 & 0 & 0 & 0 & 0 & 0 \end{bmatrix} \tag{25}$$

It is assumed that both noise vectors $w(j)$ and $v(j) = [\,v_1(j) \quad \eta_m(j)\,]^T$ are uncorrelated with zero mean.

The filter algorithm is formulated based on the system kinematics described in Eq. (1) and the measurement model defined in Eqs. (18) and (6). The prediction and update steps follow the standard Extended Kalman Filter (EKF) framework, incorporating necessary linearization and approximations. In this unconventional EKF structure, called SVD-Aided EKF, the satellite's rotational motion parameters and the attitude sensor biases are jointly estimated. The estimation process is carried out through a sequence of steps that utilize both the system model and the SVD-based attitude measurements, ensuring accurate and consistent state updates. The estimated value is found as,

$$\hat{x}(j+1) = \hat{x}(j+1/j) + K(j+1)\left\{\begin{bmatrix} Z_1(j+1) \\ Z_3(j+1) \end{bmatrix} - \begin{bmatrix} H_1\hat{x}(j+1/j) \\ h[\hat{x}(j+1/j)] + \hat{b}_m(j+1) \end{bmatrix}\right\} \tag{26}$$

The extrapolation value can be determined as,

$$\hat{x}(j+1/j) = f[\hat{x}(j)] \tag{27}$$

The filter gain of the EKF is,

$$K(j+1) = P(j+1/j)H^T(j+1)\left[H(j+1)P(j+1/j)H^T(j+1) + R(j+1)\right]^{-1} \tag{28}$$

where $H(j+1)$ is the 6×9 system measurement matrix

$$H(j+1) = \begin{bmatrix} H_{1(3\times 9)} \\ \left(\frac{\partial h[\hat{x}(j+1/j)]}{\partial \hat{x}(j+1/j)}\right)_{(3\times 9)} \end{bmatrix} \tag{29}$$

$\left(\frac{\partial h[\hat{x}(j+1/j)]}{\partial \hat{x}(j+1/j)}\right)$ is the 3×9 partial derivatives of the measurement function with respect to the states $\hat{x}(j+1/j)$, R is the covariance matrix of the SVD-Aided EKF measurement noise

$$R = \begin{bmatrix} P_{SVD} & 0_{3\times 3} \\ 0_{3\times 3} & R_m^{cor} \end{bmatrix} \tag{30}$$

The covariance matrix of the extrapolation error is,

$$P(j+1/j) = \frac{\partial f[\hat{x}(j)]}{\partial \hat{x}(j)} P(j/j) \frac{\partial f^T[\hat{x}(j)]}{\partial \hat{x}(j)} + Q(j) \tag{31}$$

The covariance matrix of the estimation error is,

$$P(j+1/j+1) = [I - K(j+1)H(j+1)]P(j+1/j) \tag{32}$$

The expressions (26)–(32) define the proposed SVD-Aided EKF for estimating the nanosatellite orientation angles and the gyroscope and magnetometer biases.

The structure of the entire algorithm using only the kinematic model is shown in Fig. 1. As can be seen, the biases of the gyro and magnetometer measurements are filtered out using the SVD-Aided EKF estimates. The bias-free rate gyro measurements are then fed back into the EKF prediction stage. The bias-free magnetometer measurements and the corrected noise covariance matrix of the magnetometer measurements are fed back into the SVD algorithm and measurement update stage of the Kalman filter, ensuring consistency and accuracy throughout the estimation process.

5. Sensor fault detection based on the trace of a Wishart matrix

If the system is working properly, then the innovation sequence of the EKF

$$\Delta(j) = \left\{ \begin{bmatrix} Z_1(j) \\ Z_3(j) \end{bmatrix} - \begin{bmatrix} H_1 \hat{x}(j/j-1) \\ h[\hat{x}(j/j-1)] + \hat{b}_m(j) \end{bmatrix} \right\} \tag{33}$$

is white Gaussian noise with zero mean and covariance

$$P_\Delta(j) = H(j)P(j/j)H^T(j) + R(j) \tag{34}$$

In the absence of measurement faults, the innovation sequence (33) will be zero mean Gaussian white noise

$$\Delta(j) \sim N_s(0, P_\Delta(j)) \tag{35}$$

Here, s denotes the dimension of the innovation sequence.

During normal operation of the measurement channels, $\tilde{\Delta}(k+1)$ normalized innovation sequence of EKF

$$\begin{aligned} \tilde{\Delta}(k) &= [P_\Delta(k)]^{-1/2}\Delta(k) \\ &= \left[H(k)P(k/k-1)H^T(k) + R(k)\right]^{-1/2}\Delta(k) \end{aligned} \tag{36}$$

will satisfy the normal distribution N(0,1) (Mehra and Peschon, 1971).

To identify sensor faults, a method based on the Wishart matrix trace is suggested. Two hypotheses are tested:

γ_0 : fault free
γ_1 : with sensor fault

It is proposed to use the normalized innovation sample covariance matrix $\hat{S}_\Delta(j)$ to detect sensor faults.

$$\hat{S}(j) = \frac{1}{M-1} \sum_{k=j-M+1}^{j} \tilde{\Delta}(k)\tilde{\Delta}^T(k) \tag{37}$$

where M is the number of realizations used (the width of the "sliding window").

The random matrix

$$A(j) = (M-1)\hat{S}(j) = \sum_{k=j-M+1}^{j} \tilde{\Delta}(k)\tilde{\Delta}^T(k) \tag{38}$$

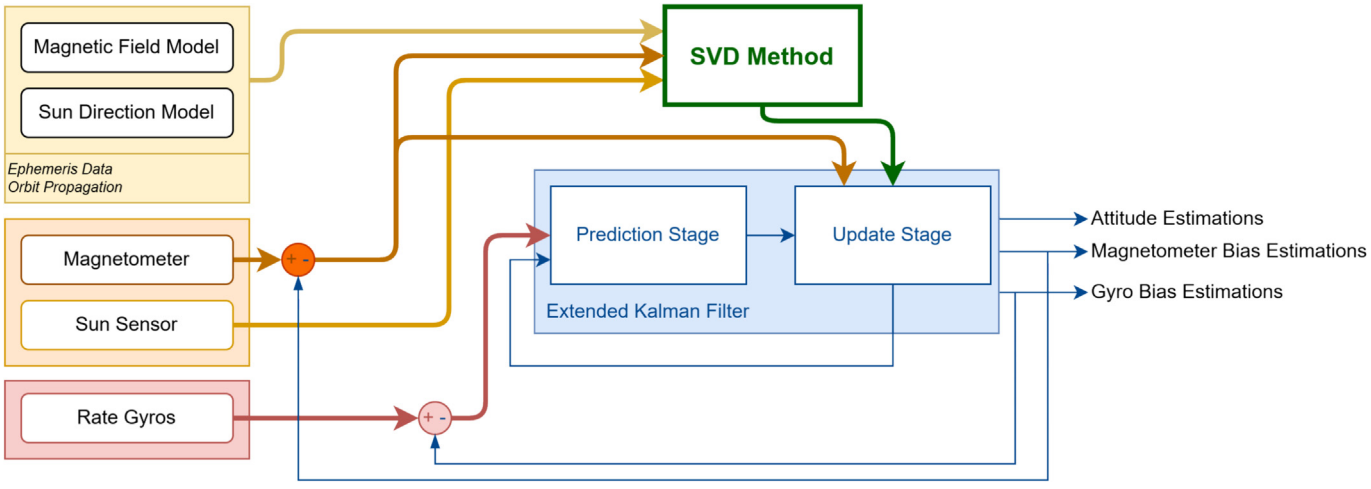

Fig. 1. SVD-Aided EKF method structure.

has a central Wishart distribution with $n = M - 1$ degrees of freedom. Consequently, the following expression can be written (Hajiyev, 2010)

$$A(j) \sim W_s(n, P_\Delta(j)) \tag{39}$$

Real-time testing of the Wishart matrix (38) is challenging due to the difficulty of determining the confidence domain of a random matrix. The trace, sum of matrix components, determinant, matrix eigenvalues, and other scalar measures of this matrix are used in practice. The diagonal elements of the random central Wishart matrix (38) can be tested using the technique described in this work. The fault detection statistic is based on the diagonal elements of the central Wishart matrix;

$$A(j) = \sum_{k=j-M+1}^{j} \widetilde{\Delta}(k)\widetilde{\Delta}^T(k) \tag{40}$$

$$diag(A(j)) = \left[\sum_{k=j-M+1}^{j}\widetilde{\Delta}_1^2(k) \quad \sum_{k=j-M+1}^{j}\widetilde{\Delta}_2^2(k) \quad . \quad \sum_{k=j-M+1}^{j}\widetilde{\Delta}_s^2(k)\right] \tag{41}$$

or

$$A_{ii}(j) = \sum_{k=j-M+1}^{j} \widetilde{\Delta}_i^2(k), \ \left(i = \overline{1,s}\right) \tag{42}$$

For $\widetilde{\Delta}_i \sim N(0, \sigma_i)$ the following expression can be written:

$$A_{ii}(j) = (M-1)\hat{\sigma}_i^2(j), \ \left(i = \overline{1,s}\right) \tag{43}$$

where $\hat{\sigma}_i^2(j)$ is the sample variance of the normalized innovation. This statistic, which is the ratio of the sample and theoretical normalized innovation variances $\hat{\sigma}_i^2/\sigma_i^2$, can be used to verify the variances of one-dimensional normalized innovations $\widetilde{\Delta}_i, \left(i = \overline{1,s}\right)$. For $\widetilde{\Delta}_i \sim N(0, \sigma_i)$, we can write

$$\frac{A_{ii}(j)}{\sigma_i^2} \sim \chi^2_{M-1}, \ \forall i, \ i = \overline{1,s} \tag{44}$$

where χ^2_{M-1} is the χ^2-distribution with $(M-1)$ degrees of freedom. For the normalized innovations the theoretical variances $\sigma_i^2 = 1, \left(i = \overline{1,s}\right)$, then the formula (44) can be rewritten in the following form:

$$A_{ii}(j) \sim \chi^2_{M-1}, \ \forall i, \ i = \overline{1,s} \tag{45}$$

Decision making for detection of sensor faults: According to the introduced hypothesis, γ_0 and γ_1 the decision rule for sensor fault detection can be written as follows:

$$\gamma_0 : A_{ii}(j) \le \chi^2_{1-\alpha,M-1} \forall i, \ i = \overline{1,s} \tag{46}$$

$$\gamma_1 : A_{ii}(j) > \chi^2_{1-\alpha,M-1} \exists i, \ i \in \overline{1,s} \tag{47}$$

When a fault affecting the variance of the normalized innovation occurs in the system, the statistics $A_{ii}(j), \ \left(i = \overline{1,s}\right)$ exceeds the threshold value $\chi^2_{1-\alpha,M-1}$ depending on the level of significance α and the degrees of freedom $(M-1)$.

6. Analysis and results

In this study, we considered a nanosatellite with mass moment of inertia $J = \text{diag}([2.1 \times 10^{-3} \quad 2.0\times \quad 10^{-3} 1.9\times 10^{-3}])$ kg.m^2 having a magnetometer, sun sensor and gyroscope as attitude and rate sensors. The nanosatellite states and gyro and magnetometer biases are estimated without using the dynamics of the satellite's rotational motion in the filter.

In the case of a single-channel magnetometer fault, SVD-Aided EKF estimates will be distorted, and consequently, magnetometer bias estimates will also be distorted. As can be seen from the structure diagram presented in Fig. 1, in this case all magnetometer channels will give faulty results, and it is not possible to determine which channel is more abnormal than the others. Therefore, in the structure shown in Fig. 1, fault isolation of sensor components (X-axis, Y-axis or Z-axis) cannot be performed using the proposed fault detection statistics.

Note that a reasonable choice of the width of the "sliding window" M is associated with the need to conduct a large volume of mathematical modeling. Too large a value of M leads to smoothing out the effects caused by faults or malfunctions in the system, too small – to an increase in the probability of false alarms. In the literature, the recommended value of M is in the range from 15 to 30. The width of the sliding window M in this study is taken to be 20. The level of significance is taken to be $\alpha = 0,05$.

6.1. Scenario 1: Estimation of attitude angles and rate gyro and magnetometer biases

Fig. 2 represents the estimation results of attitude angles by SVD-Aided EKF. As can be seen, the estimates are very close to the actual values. Figs. 3 and 4 show the errors in estimating the gyroscope bias and the variance of the errors over time. It is concluded that SVD-Aided EKF can accurately estimate the attitude angles and the bias of gyroscopes using only kinematic relations.

Corrected rate gyroscope measurements can be determined by subtracting the gyroscope bias estimates from the rate gyroscope measurements

$$Z_2^{cor}(k) = Z_2(k) - \hat{b}_g(k-1) = \omega_{BI_m}(k) - \hat{b}_g(k-1) \tag{48}$$

A comparison of the corrected rate gyro measurements with their actual values is shown in the graphs presented in Fig. 5. As can be seen, the corrected rate gyro measurements are very close to the actual values.

The variances of the corrected rate gyroscope measurement errors, calculated using formula (21), are shown in Fig. 6. As can be seen, the variances are not constant and change depending on the accuracy of the rate gyro bias estimate. Figs. 7 and 8 show the errors in estimating the magnetometer bias and the error variance.

As can be seen, the proposed method is able to accurately estimate magnetometer biases using only kinematic relations.

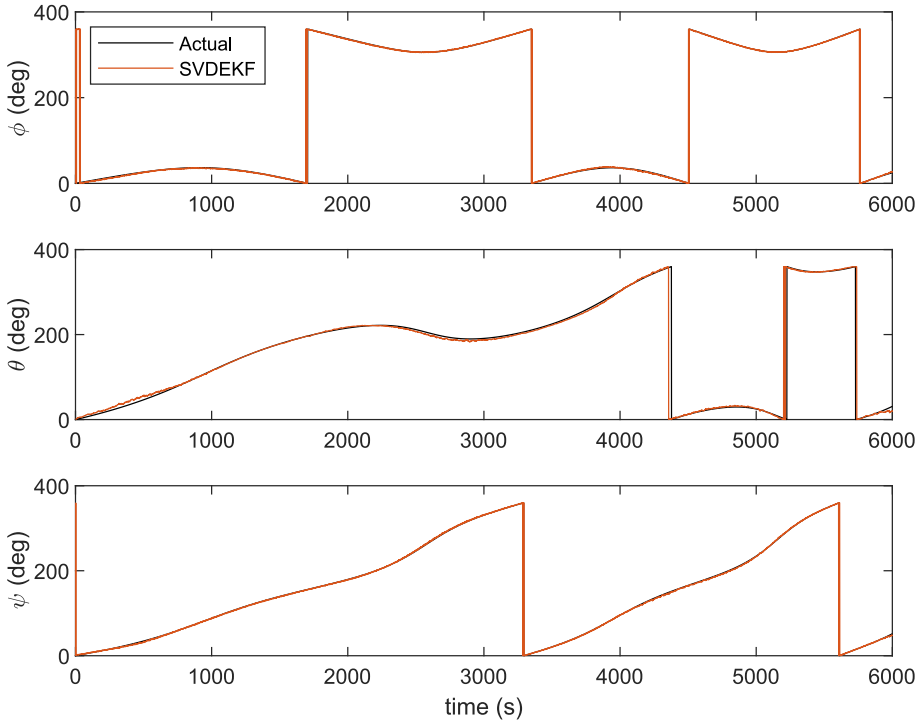

Fig. 2. Attitude angles estimation results by SVD-aided EKF.

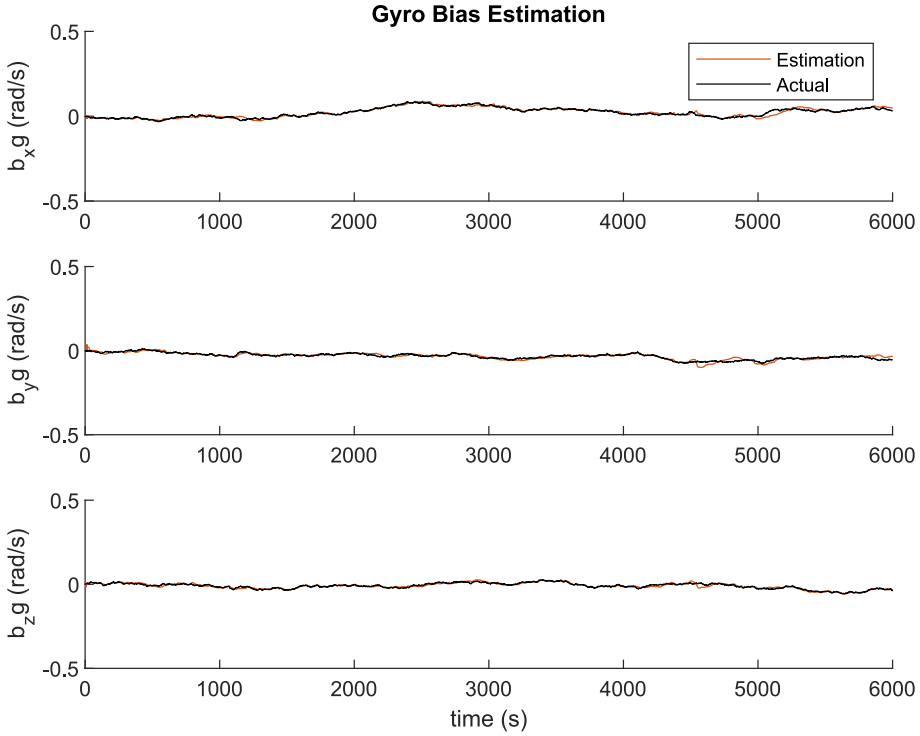

Fig. 3. Gyroscope bias estimation results by SVD-aided EKF.

Root mean square errors (RMSE) of attitude angle, angular velocity, rate gyro bias and magnetometer bias estimates obtained using the proposed SVD-aided EKF algorithm are given in Table 1.

The RMSE results show that the proposed SVD-aided EKF method provides reasonably good estimates of attitude angles and angular rates, as well as calibration of gyro and magnetometer biases.

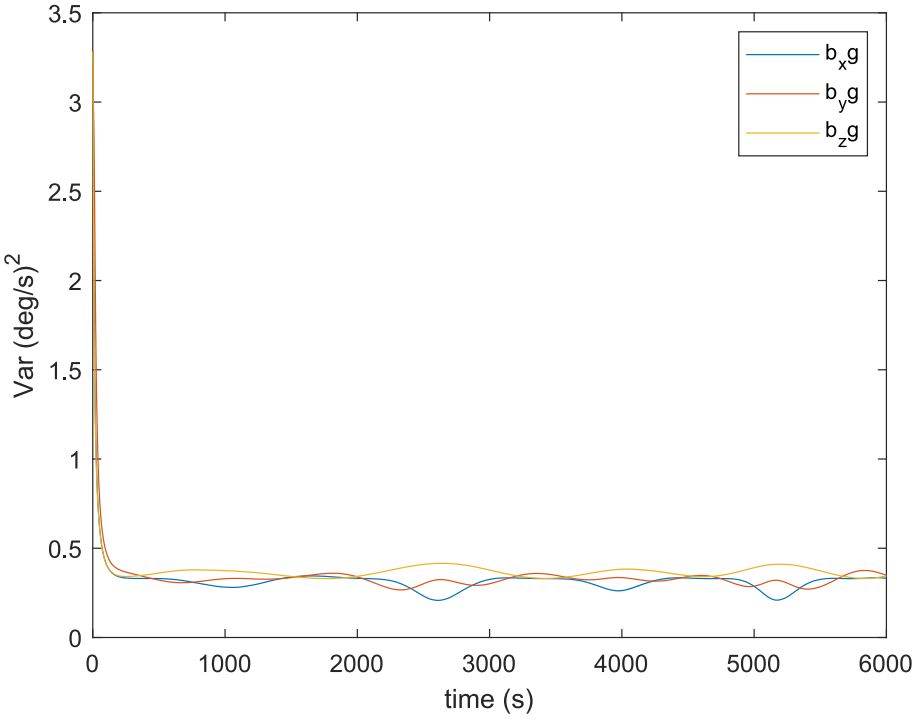

Fig. 4. Variances of gyroscope bias estimation errors by SVD-aided EKF.

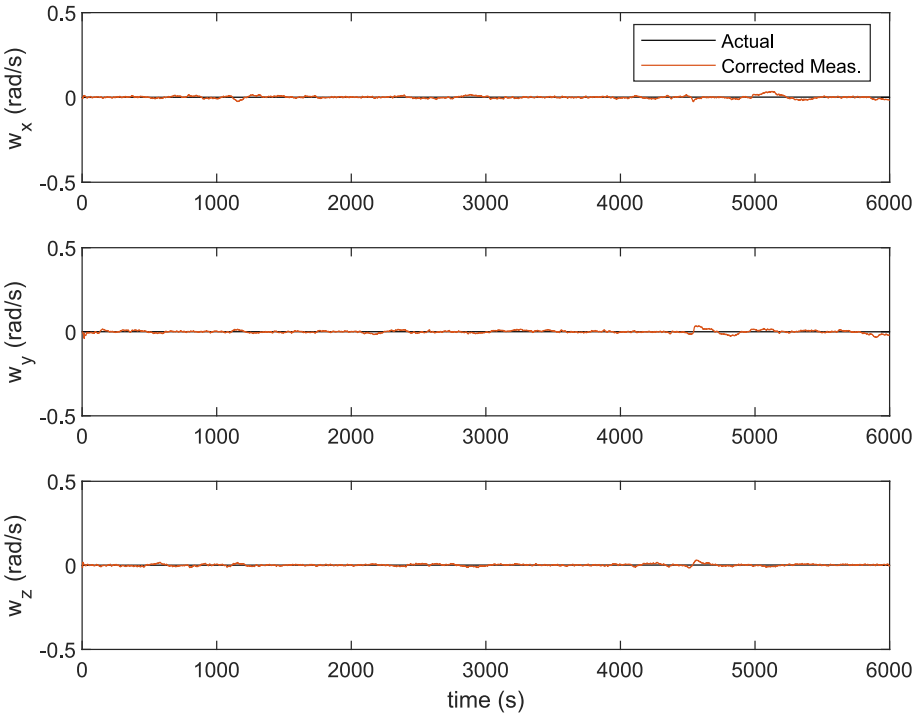

Fig. 5. Corrected rate gyroscope measurements.

6.2. Scenario 2: Magnetometer measurement noise increment

The proposed sensor fault detection algorithm based on the diagonal elements of the central Wishart matrix is used to detect a faulty attitude sensor. The measurement noise increment in the magnetometer measurements is simulated by multiplying the standard deviations of the X-axis magnetometer measurement noise by a constant number during the interval 2000–4000 s.

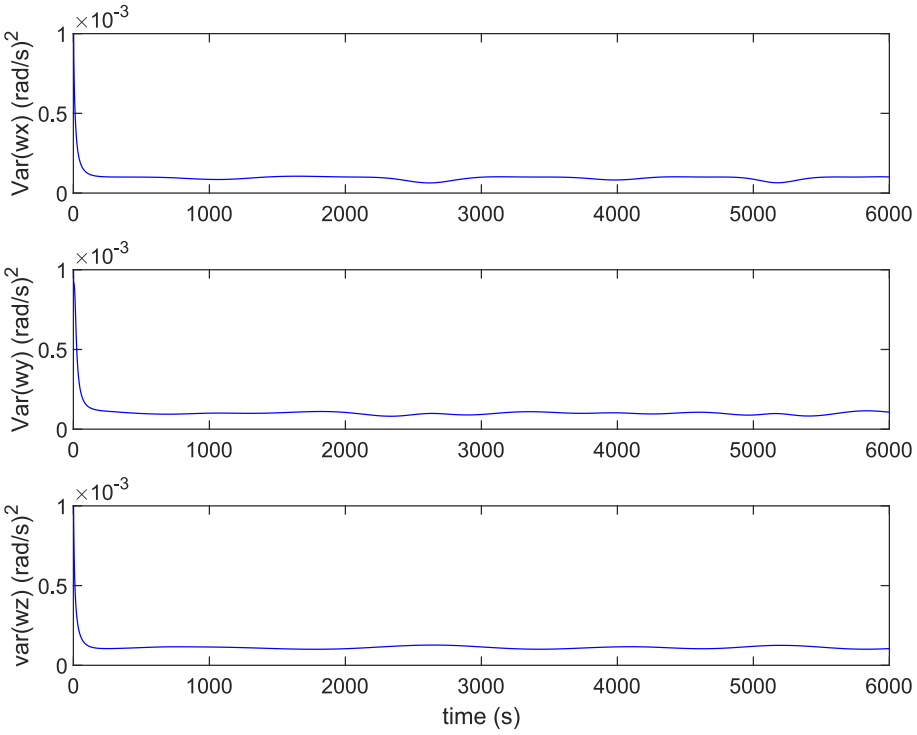

Fig. 6. Variances of the corrected rate gyroscope measurements errors.

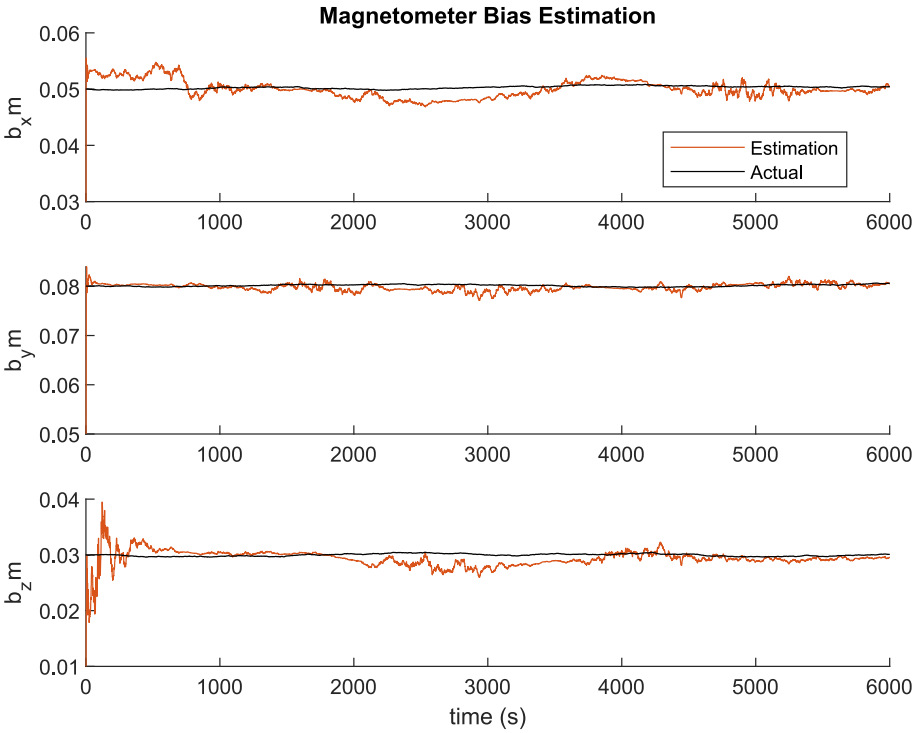

Fig. 7. Magnetometer bias estimation results by SVD-aided EKF.

$$B_{mx}(k) = AB_{ox}(k) + b_m(k) + 5\sigma_m randn, \quad (2000 \le k \le 4000) \tag{49}$$

The values of the Wishart matrix-based fault detection statistics (42) corresponding to the X-axis, Y-axis and Z-axis magnetometer measurement channels are given in Fig. 9. As can be seen from the presented graphs, the FD statistics exceed the threshold value in the faulty interval (2000–4000 s) of the X-axis magnetometer.

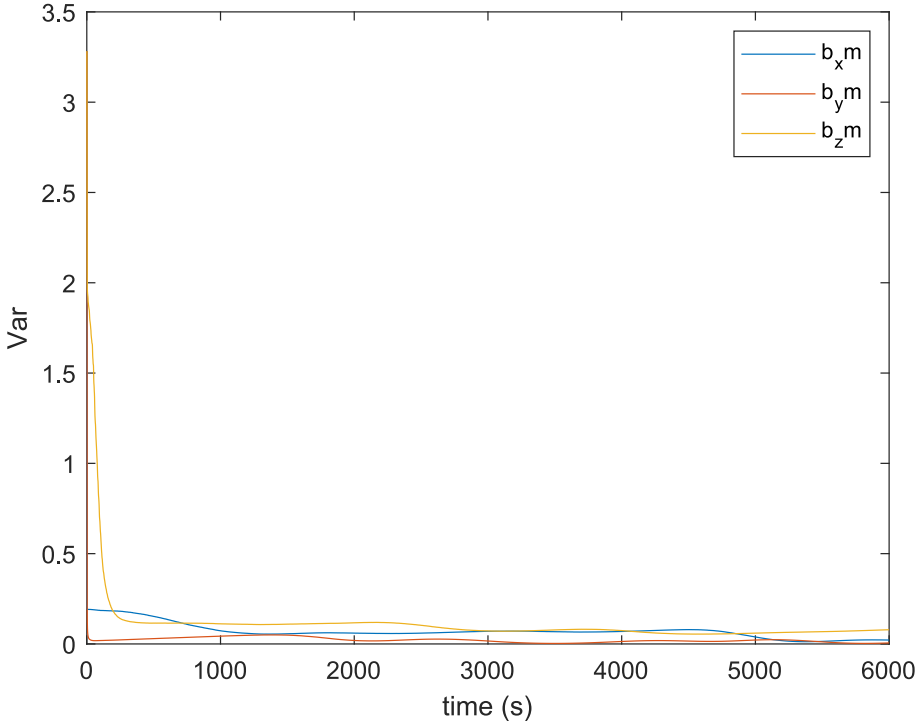

Fig. 8. Variances of magnetometer bias estimation errors by SVD-aided EKF.

Table 1
RMSE of attitude angle, angular velocity, gyro bias and magnetometer bias estimates.

Parameter	RMSE
ϕ(deg)	0.5472
θ(deg)	0.9734
ψ(deg)	0.5910
ω_x(deg/s)	0.0069
ω_y(deg/s)	0.0068
ω_z(deg/s)	0.0069
b_{g_x}(deg/s)	0.0288
b_{g_y}(deg/s)	0.0357
b_{g_z}(deg/s)	0.0227
b_{m_x}	0.0024
b_{m_y}	0.0011
b_{m_z}	0.0032

The normalized innovations corresponding to the B_x, B_y, B_z measurement channels are shown in Fig. 10 confirm the results of the FD statistics.

The values of the fault detection statistics (42) corresponding to the attitude angles determination channels are shown in Fig. 11. As can be seen from the presented graphs, the FD statistics corresponding to the yaw and roll angle determination channels exceed the threshold value in the interval of malfunction occurrence (2000–4000 s). In other words, the increase in measurement noise in the X-axis magnetometer measurements leads to failure in the attitude angle determination channels due to the use of magnetometer measurements in the SVD attitude determination algorithm.

Wishart matrix-based FD statistic values for the case of similarly increased measurement noise in the Y-axis magnetometer measurements are shown in Fig. 12. As can be seen from the presented graphs, the FD statistics exceed the threshold value in the faulty interval (2000–4000 s) of the Y-axis magnetometer.

The normalized innovations corresponding to the measurement channels B_x, B_y, B_z shown in Fig. 13 confirm the results of the FD statistics.

The proposed FD statistic values (42) for the case of similarly increased measurement noise in the Z-axis magnetometer measurements are shown in Fig. 14. As can be seen from the presented graphs, the FD statistics exceed the threshold value in the faulty interval (2000–4000 s) of the Z-axis magnetometer. According to the above fault detection decision rule, the magnetometer is considered to be faulty.

The corresponding normalized innovations presented in Fig. 15 confirm the detection of the magnetometer fault.

6.3. Scenario 3: Sun sensor measurement noise increment

The measurement noise increment in the sun sensor measurements is simulated by multiplying the standard deviations of the Y-axis sun sensor measurement noise by a constant number during the interval 2000–4000 s.

$$S_{mx}(k) = AS_{ox}(k) + 20\sigma_s randn, \quad (2000 \le k \le 4000) \qquad (50)$$

The values of the fault detection statistics (42) are given in Fig. 16. As can be seen from the presented graphs, the FD statistics corresponding to the pitch and yaw angles

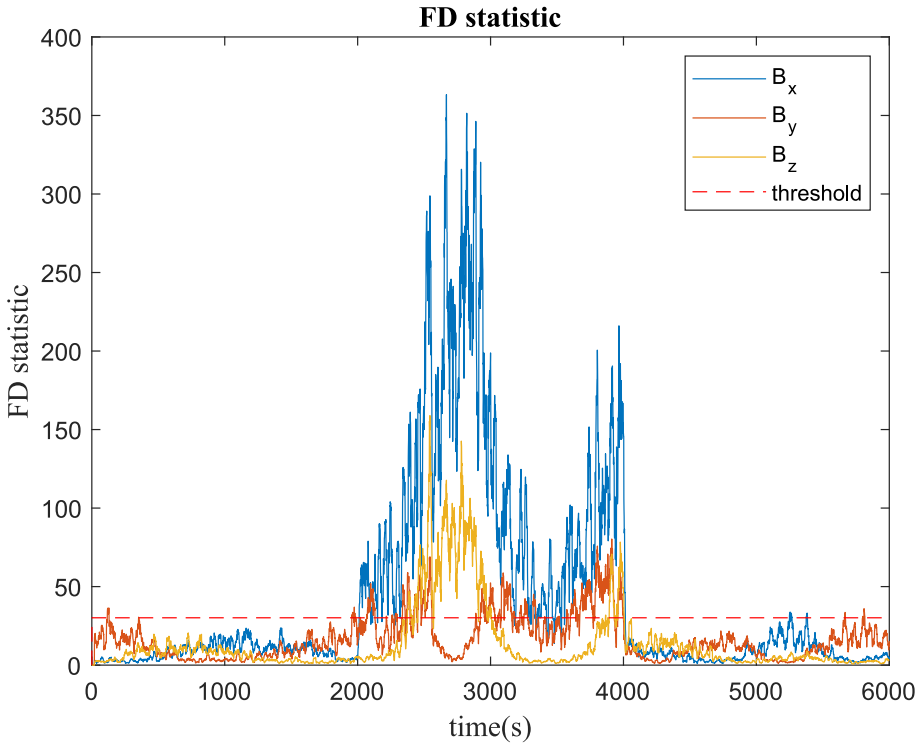

Fig. 9. Fault detection statistics for X-axis magnetometer noise increment fault.

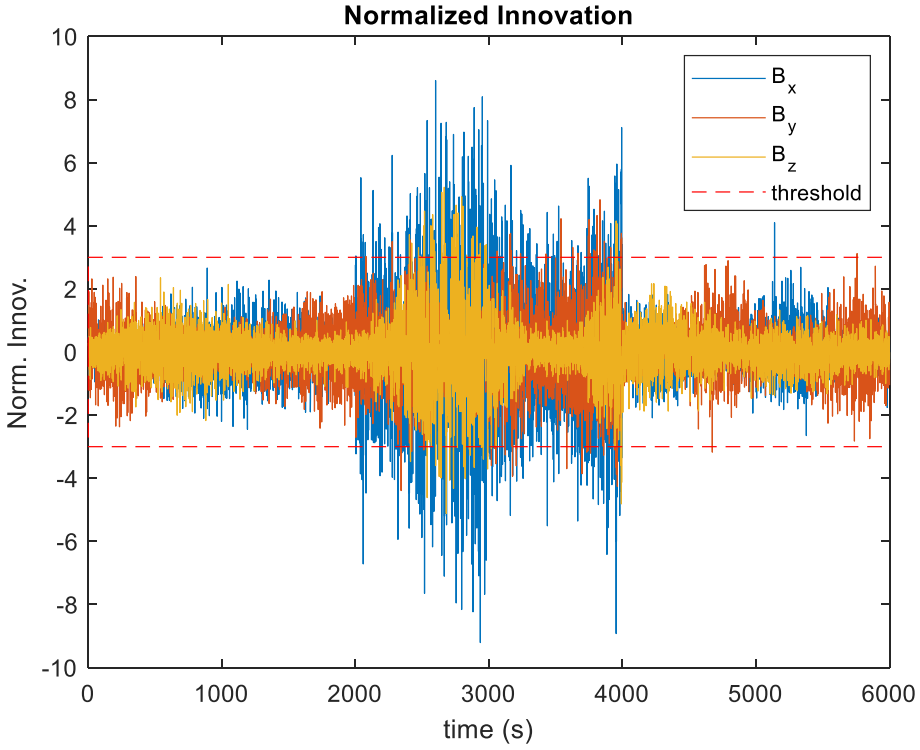

Fig. 10. Normalized innovations of magnetometer measurement channels (X-axis magnetometer noise increment fault case).

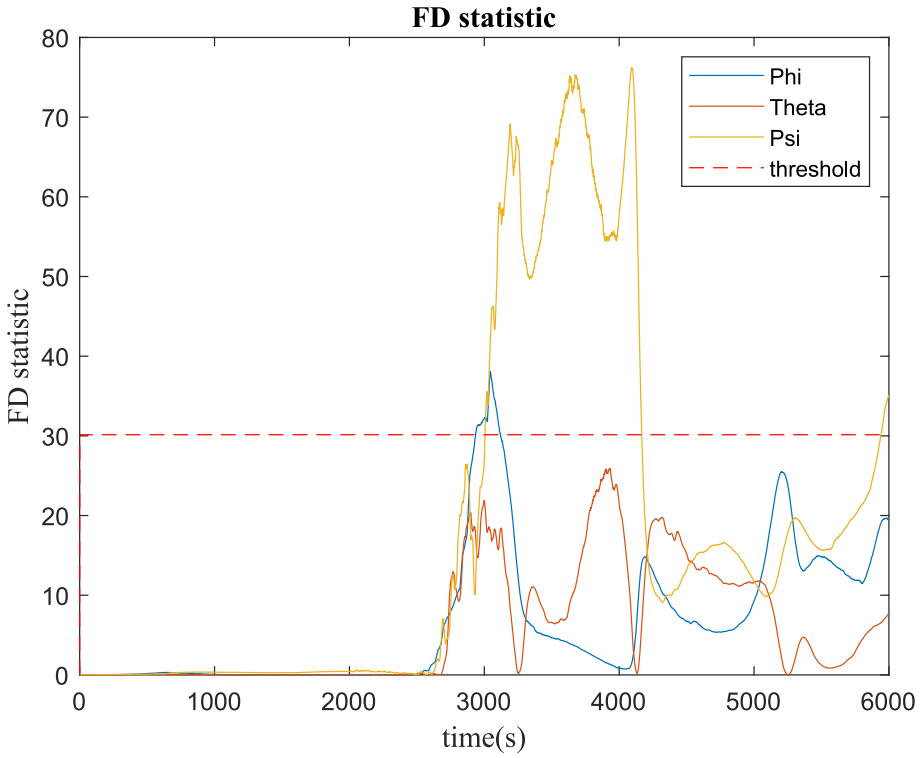

Fig. 11. Fault detection statistics for X-axis magnetometer noise increment fault.

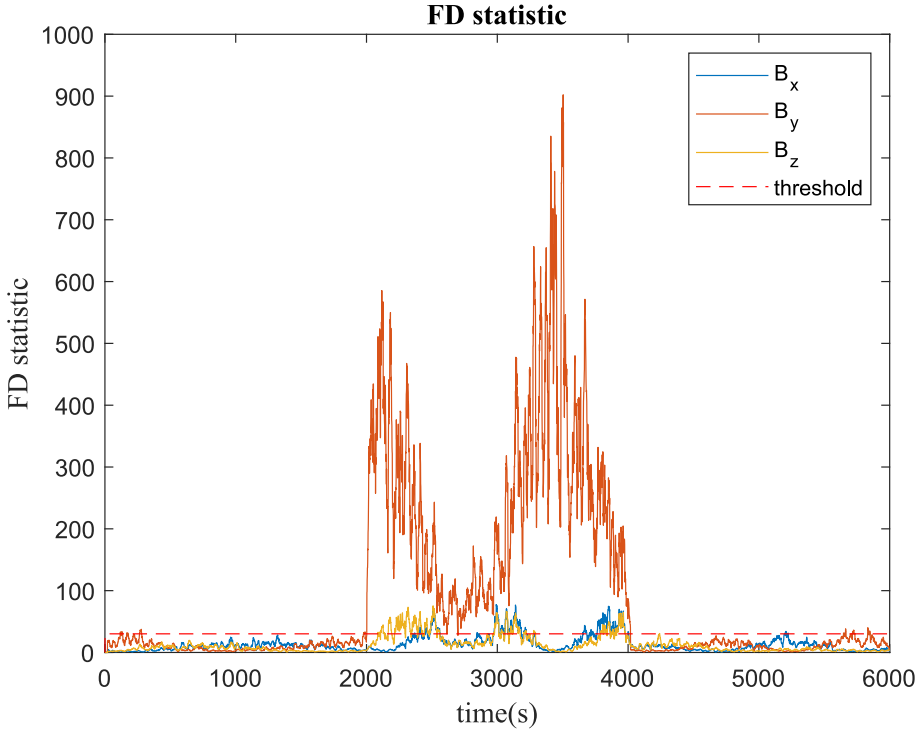

Fig. 12. Fault detection statistics for Y-axis magnetometer noise increment fault.

measurement channels exceed the threshold value in the faulty interval (2000–4000 s) of the Y-axis sun sensor. On the other hand, the magnetometer fault is not present because the FD statistics (42) corresponding to the magnetometer measurement channels along the X, Y, and Z axes are below the threshold.

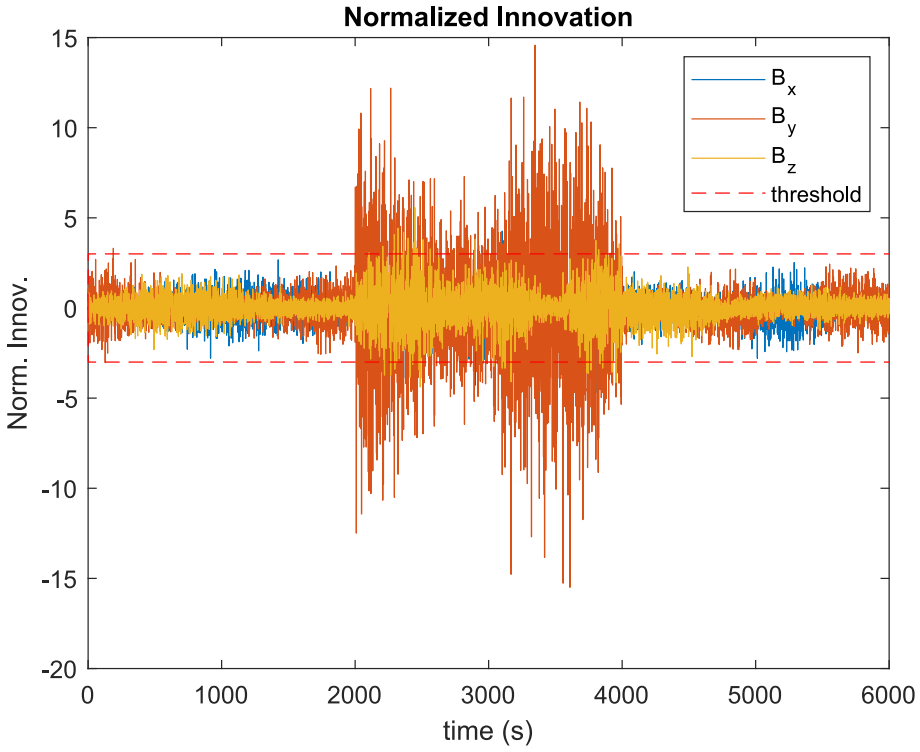

Fig. 13. Normalized innovations of magnetometer measurement channels (Y-axis magnetometer noise increment fault case).

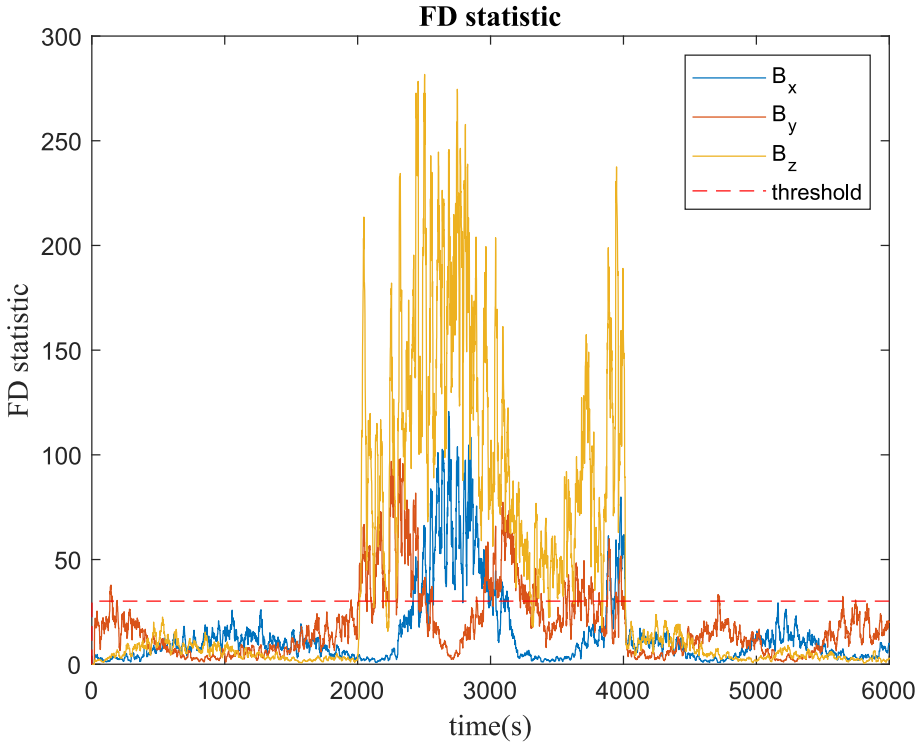

Fig. 14. Fault detection statistics for Z-axis magnetometer fault.

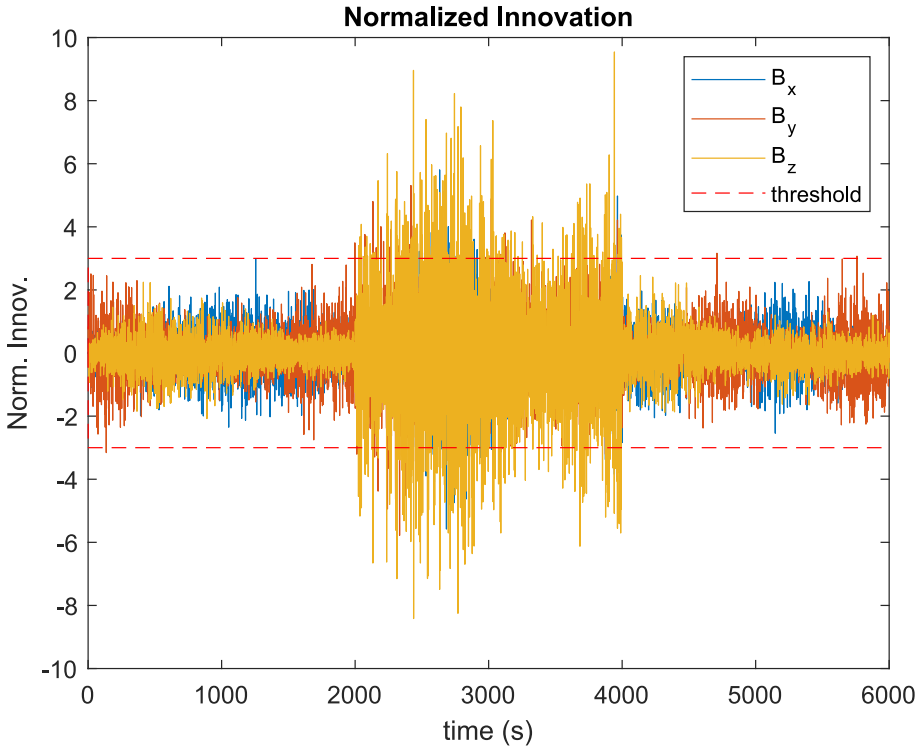

Fig. 15. Normalized innovations of magnetometer measurement channels (Z-axis magnetometer noise increment fault case).

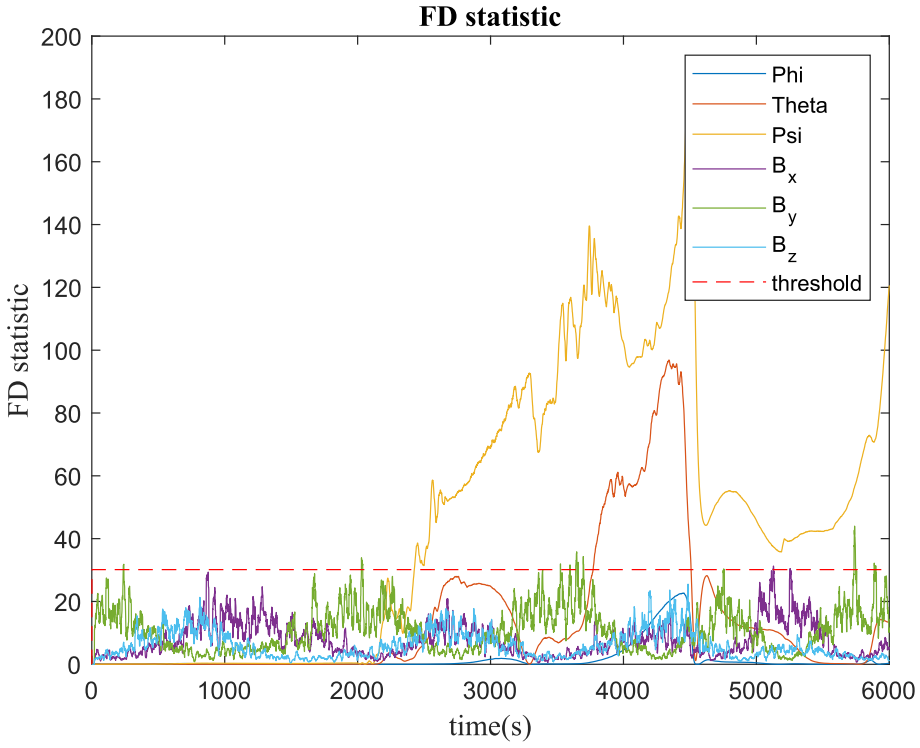

Fig. 16. Fault detection statistics for Y-axis sun sensor noise increment fault.

6.4. Scenario 4: Constant bias jumps in magnetometer measurements

In the 2000–2500 s range, a constant bias jump is added to the X-axis magnetometer measurements starting from the 2000th second of the simulation. The values of the Wishart matrix-based fault detection statistics (42) corresponding to the X-axis, Y-axis and Z-axis magnetometer measurement channels are presented in Fig. 17. As can be seen from the presented graphs, the FD statistics exceed the threshold value in the faulty interval (2000–4000 s) of the X-axis magnetometer.

As can be seen from the graphs presented in Fig. 17, the FD statistics exceed the threshold value in the faulty interval (2000–2500 s) of the X-axis magnetometer. Magnetometer bias estimation results corresponding to this case are shown in Fig. 18.

As can be seen from the graphs presented in Fig. 18, during the faulty interval of the X-axis magnetometer (2000–2500 s), the bias estimates of all three magnetometers are distorted. However, after the fault is removed, the bias estimates are corrected by the filter and approximate the true values.

6.5. Scenario 5: Magnetometer zero output fault

In the fifth measurement malfunction scenario, the measurement fault is defined as the X-axis magnetometer zero output between 2000 and 2200th sec. The fault detection statistics for this case are given in Fig. 19.

The presented graphs in Fig. 19 show that all three FD statistics exceed the threshold value in the faulty interval of the X-axis magnetometer (2000–2200 s) and according to the fault detection decision rule, the magnetometer fault is detected.

6.6. Scenario 6: Sun sensor zero output fault

In the sixth measurement malfunction scenario, the measurement fault is defined as the X-axis sun sensor zero output between 2000 and 2200th sec.

As can be seen from the results presented in Fig. 20, FD statistic corresponding to roll angle exceeds the threshold value in the faulty interval of the X-axis sun sensor (2000–2200 s). In this case, the FD statistics corresponding to the magnetometers remain below the threshold value; this corresponds to a sun sensor fault.

6.7. Scenario 7: Double sensor fault

The measurement noise increment in the X-axis magnetometer and Y-axis sun sensor measurements was simulated by multiplying the standard deviations of the sensor measurement noises in the interval 2000–2500 s by a constant number. The fault detection statistics for this case are given in Figs. 21 and 22, respectively.

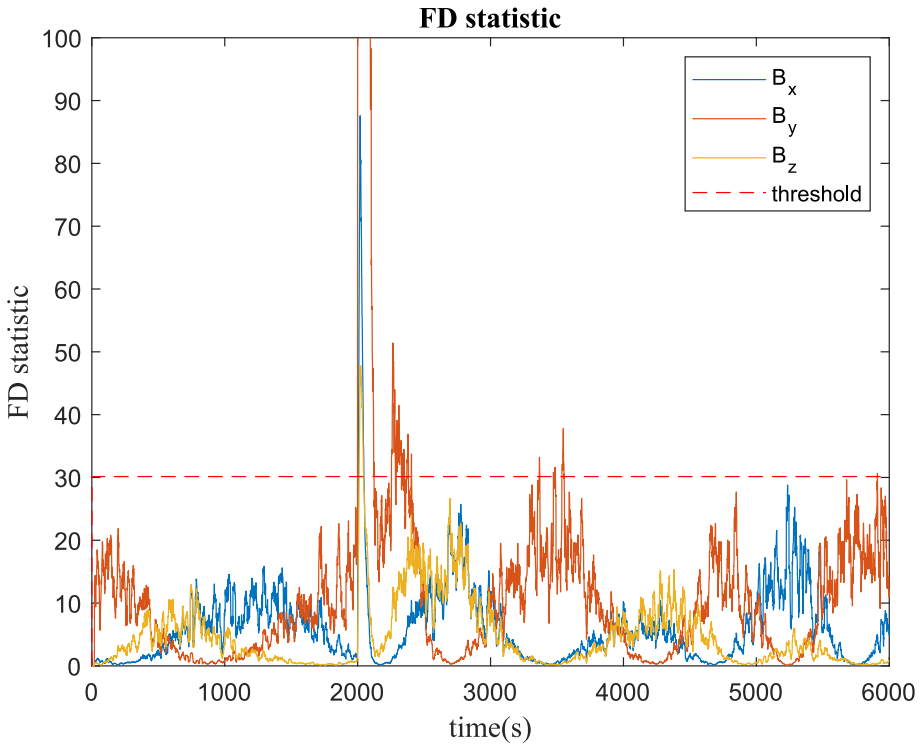

Fig. 17. Fault detection statistics for X-axis magnetometer constant bias jump fault.

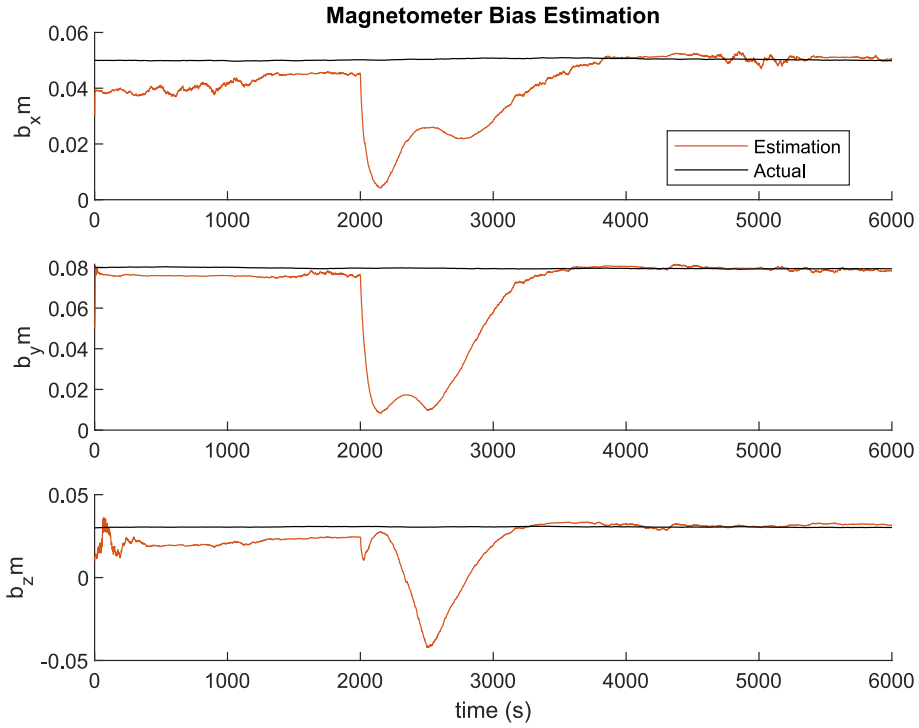

Fig. 18. Magnetometer bias estimation results for the case of constant bias jump fault in the X-axis magnetometer.

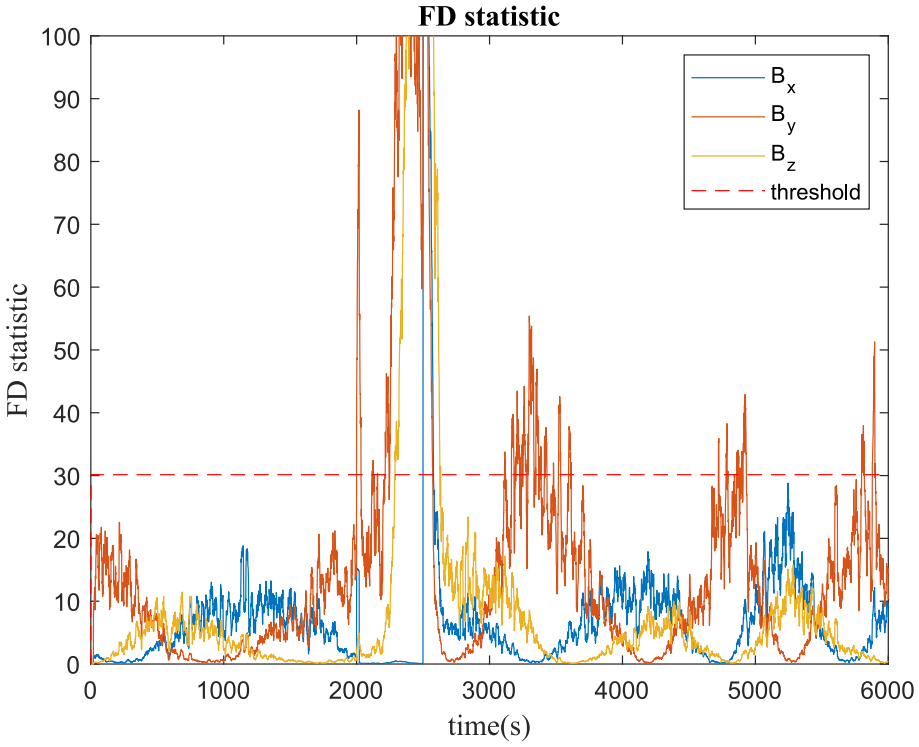

Fig. 19. Fault detection statistics for X-axis magnetometer zero output fault.

As can be seen from the presented graphs, all FD statistics corresponding to the magnetometers and the FD statistic corresponding to the yaw angle exceed the threshold value in the faulty interval (2000–2500 s) of the X-axis magnetometer and the Y-axis sun sensor.

7. Conclusions

In this study, nanosatellite attitude estimation, in-orbit calibration of attitude sensors and fault detection issues are addressed together using only kinematic relations.

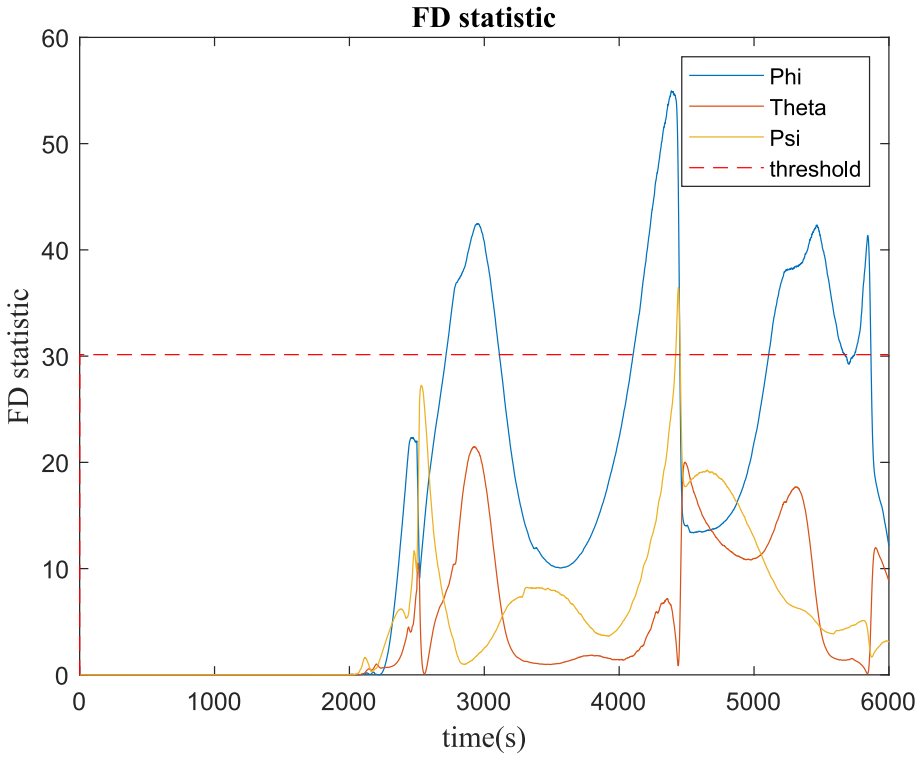

Fig. 20. Fault detection statistics for X-axis sun sensor zero output fault.

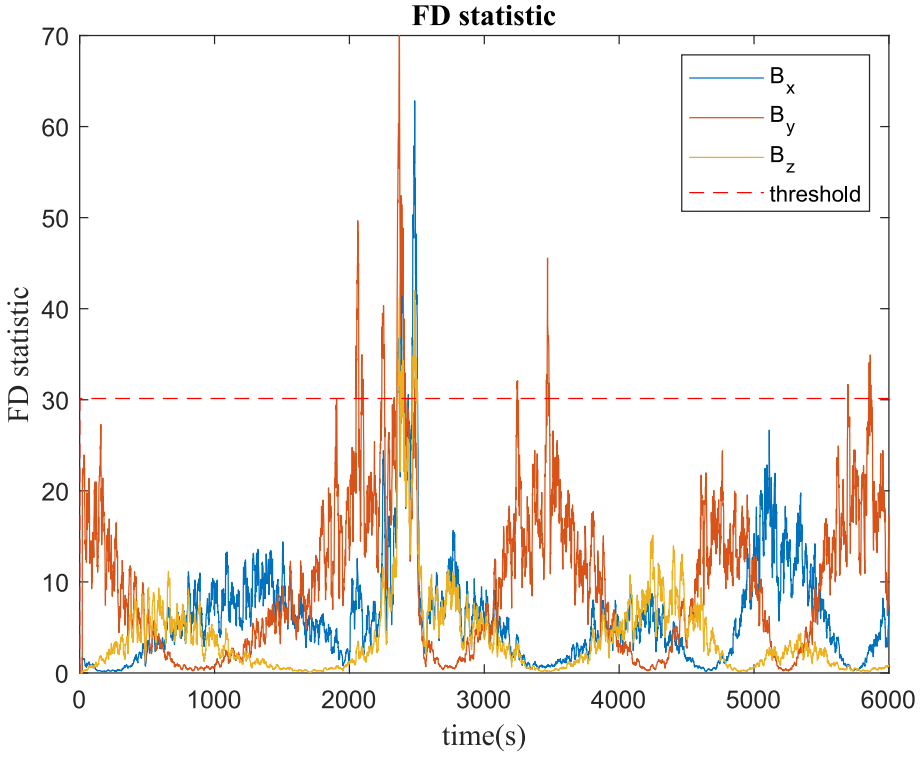

Fig. 21. Fault detection statistics corresponding to magnetometers in the case of double sensor fault.

The study presents a single-frame method-aided filter that relies solely on the kinematic equations of a nanosatellite, without the need for a dynamic model. The system integrates three onboard sensors as magnetometers, sun sensors, and gyroscopes, for attitude and rate estimation. Attitude angles are computed using a singular value

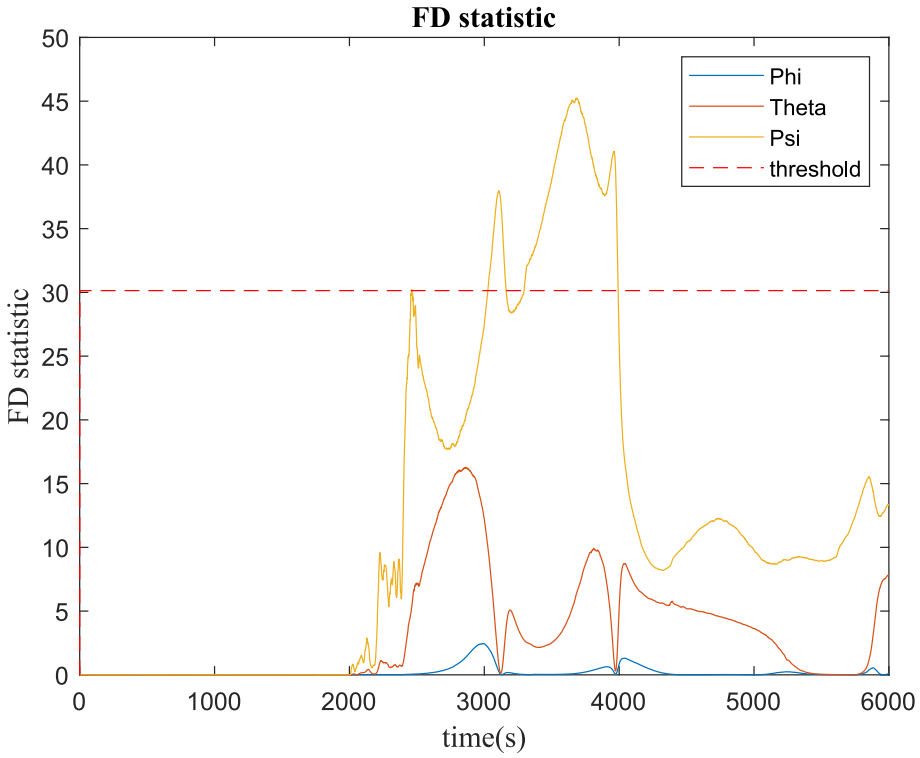

Fig. 22. Fault detection statistics corresponding to attitude angles in the case of double sensor fault.

decomposition (SVD)-based method applied to magnetometer and sun sensor data, and these estimates serve as input observations for the proposed SVD-Aided EKF. The filter simultaneously estimates the satellite's attitude and the biases in both the gyroscope and magnetometer measurements.

The problem of fault detection in attitude sensors, along with orientation estimation and sensor calibration problems, is addressed and solved. For attitude sensor fault detection, the study proposes a method based on the diagonal elements of the central Wishart matrix, derived from the innovations of the SVD-Aided EKF. The results show that the proposed framework provides accurate attitude estimation and also provides fault detection capabilities for attitude sensors for nanosatellite missions.

In the proposed combined framework for nanosatellite attitude estimation, in-orbit sensor calibration, and attitude sensor fault detection, fault isolation of sensor components (X-axis, Y-axis or Z-axis) cannot be performed using the proposed fault detection statistics. This is a drawback of the proposed method.

Future work in this area will focus on testing the developed methods at the hardware level.

Declaration of competing interest

The authors declare that they have no known competing financial interests or personal relationships that could have appeared to influence the work reported in this paper.

References

Boussadia, H., Mohammed, M.A.S., Boughanmi, N., Meche, A., Bellar, A., 2022. A combined configuration (αβ filter- TRIAD algorithm) for spacecraft attitude estimation based on in-orbit flight data. Aerosp. Syst. 5, 223–232. https://doi.org/10.1007/s42401-021-00115-9.

Cilden-Guler, D., Conguroglu, E.S., Hajiyev, C., 2017. Single-frame attitude determination methods for nanosatellites. Metrol. Meas. Syst. 24, 313–324. https://doi.org/10.1515/mms-2017-0023.

Cilden-Guler, D., Hajiyev, C., 2023. SVD-aided EKF for nanosatellite attitude estimation based on kinematic and dynamic relations. Gyroscopy Navig. 14 (4), 366–379.

Crassidis, J.L., Markley, F.L., Cheng, Y., 2007. Survey of nonlinear attitude estimation methods. J. Guid. Control. Dyn. 30, 12–28. https://doi.org/10.2514/1.22452.

Gadzhiyev, C.M., 1994. Check of the generalized variance of the Kalman filter updating sequence in dynamic diagnosis. Automat. Rem. Cont. 55, 1165–1169.

Gadzhiyev, C.M., 1996. Testing the covariance matrix of a renovating sequence under operating control of the Kalman filter. Autom. Rem. Contr. 57 (7), 1046–1052.

Gordon, B.L., 1989. Bounds for the distribution of the generalized variance. Ann. Stat. 17 (4), 1684–1692.

Hajiyev, C., 2010. Testing the covariance matrix of the innovation sequence with sensor/actuator fault detection applications. Int. J. Adapt. Cont. Sign. Proc. 24, 717–730.

Hajiyev, C., 2014. Generalized Rayleigh quotient based innovation covariance testing applied to sensor/actuator fault detection. Measurement 47, 804–812.

Hajiyev, C., Bahar, M., 2003. Attitude determination and control system design of the ITU-UUBF LEO1 satellite. Acta Astronaut. 52, 493–499. https://doi.org/10.1016/S0094-5765(02)00192-3.

Hajiyev, C., Cilden, D., 2016. Nontraditional approach to satellite attitude estimation. Int. J. Control Syst. Robot. 1, 19–28.

Hajiyev, C., Soken, H.E., 2014. Robust adaptive Unscented Kalman Filter for attitude estimation of picosatellites. Int. J. Adapt. Contr. Signal Proc. 28, 107–120. https://doi.org/10.1002/acs.2393.

Hajiyev, C., Cilden, D., Somov, Y.e., 2016. Gyro-free attitude and rate estimation for a small satellite using SVD and EKF. Aerosp. Sci. Technol. 55, 324–331. https://doi.org/10.1016/j.ast.2016.06.004.

Hajiyev, C., Cilden-Guler, D., 2021. Satellite attitude estimation using SVD-aided EKF with simultaneous process and measurement covariance adaptation. Adv. Space Res. 68, 3875–3890. https://doi.org/10.1016/j.asr.2021.07.006.

Kramlikh, A.V., Nikolaev, P.N., Rylko, D.V., 2023. Onboard two-step attitude determination algorithm for a SamSat-ION nanosatellite. Gyroscopy Navig. 14 (2), 138–153. https://doi.org/10.1134/S2075108723020050.

Lefferts, E.J., Markley, F.L., Shuster, M.D., 1982. Kalman filtering for spacecraft attitude estimation. J. Guid. Control Dynam. 5 (5), 417–429. https://doi.org/10.2514/3.56190.

Liu, N., Qi, W., Su, Zh., Feng, Q., Yuan, Ch., 2022. Research on gradient-descent extended Kalman attitude estimation method for low-cost MARG. Micromachines 13, 1283. https://doi.org/10.3390/mi13081283.

Markley, F.L., Crassidis, J.L. Cheng, Y., 2005. Nonlinear attitude filtering methods. In: AIAA Guidance, Navigation, and Control Conference and Exhibit. San Francisco, California.

Markley, F.L., Mortari, D., 2000. Quaternion attitude estimation using vector observations. J. Astronaut. Sci. 48, 359–380.

Mehra, R.K., Peschon, J., 1971. An innovations approach to fault detection and diagnosis in dynamic systems. Automatica 7, 637–640.

Mmopelwa, K., Ramodimo, T.T., Matsebe, O., Basutli, B., 2023. Attitude determination system for a cubesat experiencing eclipse. Sensors 23, 8549. https://doi.org/10.3390/s23208549.

Soken, H.E., Sakai, S., 2019. Triad+ filtering approach for complete magnetometer calibration. In: 9th International Conference on Recent Advances in Space Technologies (RAST-2019), Istanbul, Türkiye. IEEE, pp. 703–708.

Wertz, J.R., 2002. Spacecraft Attitude Determination and Control. Astrophysics and Space Science Library. D.Reidel Publishing Company, Dordrecht, Holland.

Zhang, S., Chang, G., Chen, Ch., Zhang, L., Zhu, T., 2020. Attitude determination using gyros and vector measurements aided with adaptive kinematics modeling. Measurement 157, 107679. https://doi.org/10.1016/j.measurement.2020.107679.